Ultramicroscopy 279 (2026) 114260

Contents lists available at ScienceDirect

Ultramicroscopy

journal homepage: www.elsevier.com/locate/ultramic

Experimental study of energy-dependent angular broadening of MeV electron beams for high-resolution imaging in thick samples

Xi Yang [a,*], Paul Denham [b], Atharva Kulkarni [b], Brian Schaap [b], Victor Smaluk [a], Tianyi Wang [a], Nathalie Bouet [a], Mourad Idir [a], Pietro Musumeci [b]

[a] National Synchrotron Light Source II, Brookhaven National Laboratory, Upton, NY 11973, USA
[b] Department of Physics and Astronomy, UCLA, Los Angeles, California 90095, USA

ARTICLE INFO

Keywords:
MeV-STEM
Energy-dependent angular broadening
Electron-sample interaction
Analytical model and Monte Carlo simulation
Nano-imaging thick biological samples
Electron beam parameters

ABSTRACT

In scanning transmission electron microscopy (STEM), spatial resolution is primarily influenced by the projected size of the electron probe within the specimen. In thin samples, a large semi-convergence angle enables a tightly focused beam and sub-nanometer resolution. However, in thick specimens, resolution is fundamentally limited by transverse beam broadening from multiple large-angle scattering events—for example, a probe with 10 mrad angular divergence can broaden by ~100 nm over a 10 μm path. Since this broadening scales inversely with beam energy, MeV-STEM offers a promising route for high-resolution imaging in thick materials. To quantitatively assess this effect, we performed high-precision measurements at UCLA's PEGASUS beamline, characterizing beam divergence and intensity profiles for 3–8 MeV electrons transmitted through a wedged-silicon sample of varying thickness. Our results reconcile discrepancies among analytical models and validate Monte Carlo simulations. We find that increasing beam energy from 3.0 to 5.8 MeV reduces angular broadening by a factor of 2.6, with diminishing returns observed at 7.6 MeV. These findings provide a quantitative framework for optimizing MeV-STEM parameters in high-resolution imaging of thick biological and microelectronic specimens, and for guiding beam energy selection in other advanced imaging modes beyond STEM.

1. Introduction

High-resolution imaging of thick biological specimens in their native states, such as the densely packed networks of DNA, RNA, and proteins within the cell nucleus, remains a fundamental challenge in electron microscopy due to strong multiple scattering and the limited penetration of conventional low-energy electron beams [1]. Mega-Electron-Volt Scanning Transmission Electron Microscope (MeV-STEM) has recently emerged as a promising solution, enabling imaging of specimens several micrometers thick [2]. By utilizing high-energy electrons (≥3 MeV), MeV-STEM offers increased penetration depth, enhanced amplitude contrast, reduced radiolysis damage in biological specimens, and minimal sample preparation artifacts [3–6], although knock-on displacement and sputtering may arise in crystalline or inorganic systems. These capabilities enable nondestructive, high-throughput imaging across a broad range of materials, with biological tissues and microelectronic devices being particularly relevant examples. Recent advances in photocathode design and superconducting RF acceleration technologies have been key to realizing this progress [2,7–13].

Despite these advantages, spatial resolution in thick samples remains constrained by transverse beam broadening due to multiple large-angle scattering events [2,7,8,14]. This broadening increases with sample thickness and decreases with beam energy, creating a performance tradeoff that limits achievable resolution. A quantitative understanding of energy-dependent angular scattering is thus essential for optimizing MeV-STEM imaging in thick, scattering-dominated media.

In this work, we present a combined experimental and computational investigation of angular broadening across the 3–8 MeV energy range. Using quantitative measurements at the PEGASUS beamline (UCLA), we characterize beam divergence through silicon up to 20 μm thick. Experiments with wedged silicon samples validate analytical and numerical models. We find that angular broadening decreases significantly with increasing beam energy (from 3.0 to 5.8 MeV), while further increases within the range we tested yield diminishing returns. These findings establish a quantitative basis for optimizing MeV-STEM and guide energy selection across imaging modes beyond STEM for high-

* Corresponding author.
E-mail address: xiyang@bnl.gov (X. Yang).

https://doi.org/10.1016/j.ultramic.2025.114260
Received 2 August 2025; Received in revised form 21 September 2025; Accepted 18 October 2025
Available online 18 October 2025

resolution imaging of thick materials, including but not limited to biological and microelectronic specimens.

2. Results

To quantitatively characterize MeV-electron interactions with solid samples, we developed a systematic framework integrating sample preparation, accelerator tuning, beam diagnostics, and data analysis. The procedure comprises five key stages: (1) sample fabrication, (2) accelerator configuration, (3) beam divergence measurement, (4) data processing and interpretation, and (5) standardization of procedures for quantifying beam–sample interactions. This reproducible methodology addresses a critical gap in the empirical validation of analytical scattering models and Monte Carlo (MC) simulations. Analytical models provide compact scaling laws based on approximate scattering cross-sections, enabling rapid estimates across energies and materials. In contrast, MC simulations stochastically sample individual scattering events from evaluated cross-sections, capturing full angular distributions with higher fidelity. Together, these complementary approaches provide a robust foundation for benchmarking scattering models and optimizing nondestructive MeV-STEM imaging of thick biological and functional materials.

2.1. Sample fabrication and characterization

To enable controlled investigation of MeV-electron scattering, we fabricated a wedge-shaped silicon sample with a precisely defined thickness gradient [18]. A 30 mm × 15 mm × 20 μm silicon wafer, representative of microelectronic and advanced material systems, served as the substrate. The wedge geometry, ranging continuously from 0.2 μm to 20.0 μm, was formed using the Ion Beam Figuring (IBF) method [18–20], yielding a reproducible, linear thickness gradient (see Supplementary Information for additional sample fabrication details).

Thickness mapping by interferometry [21,22] revealed a uniform gradient of 2 μm/mm across the 7.5 mm horizontal scan range used in measurements (Fig. 1). This well-defined geometry provided a high-fidelity reference for systematic scattering studies at the PEGASUS beamline, enabling rigorous validation of models and optimization of MeV-STEM imaging for thick specimens.

2.2. Accelerator configuration

Experiments were performed at the Pegasus electron accelerator facility at UCLA [15–17], which provides a tunable beam energy from 3 MeV to 8 MeV, well-suited for studying energy-dependent angular broadening in MeV electron–matter interactions. A detector configuration, guided by prior simulations [18], was implemented to measure beam intensity and divergence with high spatial and angular resolution.

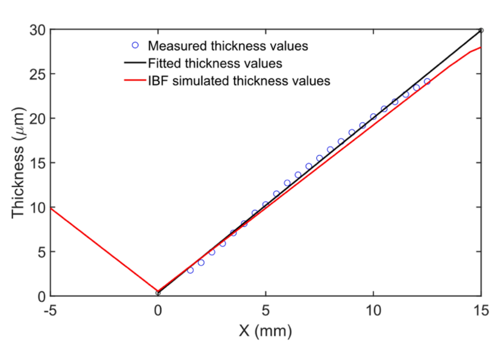

Fig. 1. Thickness profile of the wedge-shaped silicon sample: simulated gradient from the IBF process (red line) and interferometric measurements (blue circles). The fitted slope (black line) confirms a uniform 2 μm/mm gradient.

To accurately resolve the angular spread, 20 μm-thick YAG scintillators with high spatial resolution [23] were strategically positioned at multiple downstream locations (Table 1). Detector locations were optimized to ensure the full beam profile remained within the active area of each screen, minimizing clipping and measurement artifacts. At the lowest beam energy (3 MeV), where divergence is greatest, Screen 1a was repositioned upstream to preserve angular resolution and prevent beam overspill. This experimental configuration enabled accurate, angle-resolved measurements of beam divergence as a function of energy and sample thickness, supplying essential benchmarks for testing scattering models. A schematic of the PEGASUS beamline is shown in Fig. 2.

2.3. Theoretical and analytical framework

This study aims to validate both analytical [8,24,25] and Monte Carlo simulation models [18,26] by comparing their predictions with experimental data obtained from the PEGASUS beamline. Although PEGASUS does not provide energy-resolved detection, inelastic scattering can be reasonably neglected when modeling angular broadening of MeV electrons in light to medium-$\widetilde{Z}$ materials, as its contribution to angular deflection is negligible compared to elastic scattering. This assumption is further supported by the use of a silicon sample, where the characteristic angle from elastic interactions is approximately 200 times larger than that from inelastic processes (see Table 2), effectively isolating the elastic contribution.

To quantify elastic scattering, we employ two established analytical models for the differential cross-section: (1) the Wentzel formalism (based on the screened Rutherford potential under the first-Born approximation) [8]; and (2) the classical Rutherford-Mott model [24], which incorporates relativistic corrections via the Mott factor. These formalisms yield energy-dependent characteristic scattering angles, defined as the polar angles encompassing 50 % of elastically scattered electrons. The Wentzel model provides more accurate predictions for screened interactions in the MeV regime, while the Rutherford-Mott model serves as a classical reference baseline. The predicted elastic scattering angles from both models, along with the inelastic angle derived from the Bethe formalism, are summarized in Table 2.

To connect these models with experimental observables, we define the increase in angular divergence relative to the thinnest region as

$$f(\Delta t) = \Theta(t) - \Theta(t_{min}), \quad (1)$$

where $\Theta(t)$ denotes the angular divergence (equivalent to $\sigma_\theta(t)$), f corresponds to the increment $\Delta\sigma_\theta$, $\Delta t = t - t_{min}$, and $t_{min} \approx 0.2\ \mu m$.

For a screen at distance Z from the sample, the beam size is

$$\sigma_x(t) = \sqrt{\sigma_x(t_{min})^2 + (f(\Delta t) \cdot Z)^2}, \quad (2a)$$

which can be rearranged as

Table 1
Scintillator screen configurations for beam divergence measurements. Screens 1, 1a, and 1b were positioned downstream of the silicon sample at distances Z (sample exit to detector surface). Calibration values are in μm/pixel. Collection angle indicates the maximum detectable beam divergence relative to the optical axis. 20 μm-thick YAG screen offers ~2 μm spatial resolution [23]. Screens 1 was used at 5.8 and 7.6 MeV; screens 1a and 1b at 3.0 MeV.

Screen	Z (mm)	Calibration (μm/pixel)	Collection angle (mrad)	Type	Used by
1	210	10	6	YAG	$E = 5.8$, 7.6 MeV
1a	90	11.11	14	YAG	$E = 3.0$ MeV
1b	194	10	> 14	fluorescence	$E = 3.0$ MeV

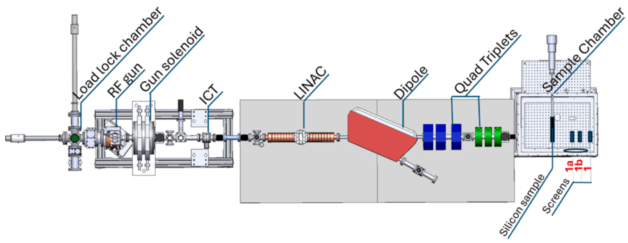

Fig. 2. Schematic of the PEGASUS beamline for angular broadening measurements. The silicon wedge sample is mounted in the sample chamber. Measurement screens 1a, 1b, and 1 are shown (see Table 1 for details).

$$\sigma_x(t)^2 - \sigma_x(t_{min})^2 \approx f(\Delta t)^2 \cdot Z^2 = p_1 \cdot \Delta t^2 + p_2 \cdot \Delta t + p_3, \tag{2b}$$

where p_1, p_2, and p_3 are the second-, first- and zeroth-order polynomial coefficients, respectively, as shown in the Fig. 4a caption; by construction, $p_3 = 0$ at $t = t_{min}$. Although these coefficients are not themselves of physical interest, the quadratic form provides a convenient way to extract the angular broadening rate:

$$\frac{d\Theta}{dt}(t) = \frac{df(\Delta t)}{d\Delta t} = \frac{d\sqrt{\sigma_x(t)^2 - \sigma_x(t_{min})^2}}{Z\, dt} = \frac{1}{Z}\frac{p_1\Delta t + p_2/2}{\sqrt{p_1\Delta t^2 + p_2\Delta t}} \tag{3}$$

To quantify multiple elastic scattering, we apply the Highland formula [25] for the RMS scattering angle of an electron with momentum p and normalized velocity $\beta = \frac{v}{c}$ after traversing thickness t:

$$\Theta(t) \approx \frac{13.6\ MeV}{\beta \cdot p \cdot c} \cdot \sqrt{\frac{t}{X_0}} \cdot \left[1 + 0.038 \cdot ln\left(\frac{t}{X_0}\right)\right], \tag{4}$$

with the radiation length X_0=9.36 cm for silicon [26]. The constant 13.6 MeV arises from a fit to Molière's multiple scattering theory and is documented by the Particle Data Group [27].

Differentiating Eq. (4) with respect to t and neglecting higher order terms in t/X_0yields the angular broadening rate per unit thickness:

$$d\Theta \Big/ dt \approx \frac{13.6\ MeV}{\beta \cdot p \cdot c} \cdot \frac{1.076 + 0.038 \cdot ln(t/X_0)}{2\sqrt{(t \cdot X_0)}}. \tag{5}$$

For comparison with the experiment, analytical predictions are based on these scaling laws (Eqs. (4) and 5), whereas MC simulations provide higher-fidelity angular distributions by stochastically sampling individual scattering events. A general discussion of the advantages of each approach is provided in Section 2.

2.4. Experimental measurements

Building on the theoretical framework described in Section 2.3, we performed systematic measurements of beam divergence at electron energies (kinetic) of 3.0, 5.8, and 7.6 MeV using precision-fabricated silicon wedge samples. A low-divergence beam (~3 mrad semi-convergence) was produced by focusing downstream of the sample, minimizing initial angular spread and improving measurement accuracy. Although the broadening is largely unaffected by variations in incident angle within the experimental range (Section 2.6.1), this configuration ensured consistent and reliable data. The root mean square (RMS) beam size was much smaller than the active area of both Screen 1 and Screen 1a, with the entire beam profile confined within the YAG scintillator. On-sample beam size remained below 1 mm, allowing accurate positioning within the 5 mm uniformly thick sample region.

The experimental procedure began with horizontal motorized scanning to concurrently minimize the beam size and maximize its intensity on Screen 1 or 1a, followed by vertical alignment based on the same criteria. Once optimized, the vertical position was fixed for the remainder of the experiment. Scanning proceeded from the thick end of the wedge toward the thinnest point ($t_{min} \approx 0.2\ \mu$m), defined by interferometric mapping and set as the origin ($X = 0$), and then into the positive gradient direction. As expected, the beam size reached a minimum at t_{min} and increased with s thickness thereafter (Fig. 3a).

Beam conditions were carefully stabilized throughout the scans: the energy spread was minimized ($\frac{\sigma_E}{E} \leq 10^{-3}$) by tuning of the drive laser intensity and the RF phases of the accelerating cavities; the beam charge was maintained near 1 pC to ensure sufficient image intensity; and trajectory steering ensured beam passage through the centers of all measurement screens. The horizontal scan range was chosen to maintain the integrated beam intensity above 90 % of peak (Fig. 3b). Each scan consisted of 150 steps over a 7.5 mm range with a 50 μm step size; motor repeatability was within 1 μm. At each step, ten images were recorded for statistical averaging. A full scan took approximately 25 min, during which no measurable drift in beam parameters was observed. Measurements were performed using 20 μm-thick YAG:Ce scintillators, and images showing partial beam clipping were excluded from analysis.

Fig. 3 summarizes the raw measurements. The motor position $X =$ 0 was defined by interferometric mapping prior to measurement and corresponds to the scan position of minimum beam size. Negative positions appear because the IBF-processed region extended beyond the [0, 15] mm mapping span; however, this side was not intentionally fabricated and is less well controlled, which explains the small asymmetries visible in Fig. 3b For this reason, quantitative analysis is restricted to the positive side. The horizontal coordinate Δt denotes the thickness increment relative to the thinnest point, and dual horizontal axes (motor position and thickness) are provided for clarity.

Fig. 3a shows the horizontal beam size σ_x for each energy, with the top axis denoting thickness and the bottom axis motor position. Distinct markers denote the different energies: red stars for 3.0 MeV at Screen 1a, magenta squares for 5.8 MeV at Screen 1, and blue circles for 7.6 MeV at Screen 1. Solid lines indicate the averaged trends, while the spread in σ_x reflects statistical uncertainty from ten repeated measurements per point. Beam sizes measured at Screen 1b were scaled by the geometric factor Z_{s1a}/Z_{s1b}, where Z_{s1a} and Z_{s1b} denote the distances from the sample exit to Screen 1a and 1b, respectively, as listed in Table 1 and projected onto the Screen 1a plane; since the results agreed well and added no further insight, they are omitted from Fig. 3a for clarity.

Fig. 3b shows normalized transmitted intensity, which remained

Table 2
Critical scattering angles and angular broadening rates for electrons in silicon at 3.0–7.6 MeV. θ_{el} and θ_{inel} are the critical elastic and inelastic scattering angles estimated via the Wentzel and Bethe models, respectively. $\theta_{el,R}$ is the elastic angle from the classical Rutherford model [24]. Broadening rates $d\Theta_{meas}/dt$ and $d\Theta_{model}/dt$ are from experiment and analytical estimates (Highland formula [25]), evaluated at $t = 1\ \mu m$ and averaged over the range $t = 1 - 6\ \mu m$.

Electron Energy E (MeV)	Elastic critical angle θ_{el} (mrad)	Inelastic critical angle θ_{inel} (mrad)	Rutherford modeled critical angle $\theta_{el,R}$ (mrad)	Measured broadening rate $d\Theta_{meas}/dt$ (mrad/μm)		Highland Modeled broadening rate $d\Theta_{model}/dt$ (mrad/μm)	
				$t = 1\ \mu m$	$Mean(1\ to\ 6$ μm)	$t = 1\ \mu m$	$Mean(1\ to\ 6$ μm)
3.0	2.588	0.011	0.436	4.758	2.780	4.145	2.647
5.8	1.429	0.006	0.226	1.818	1.045	2.258	1.443
7.6	1.110	0.005	0.170	1.217	0.838	1.766	1.130

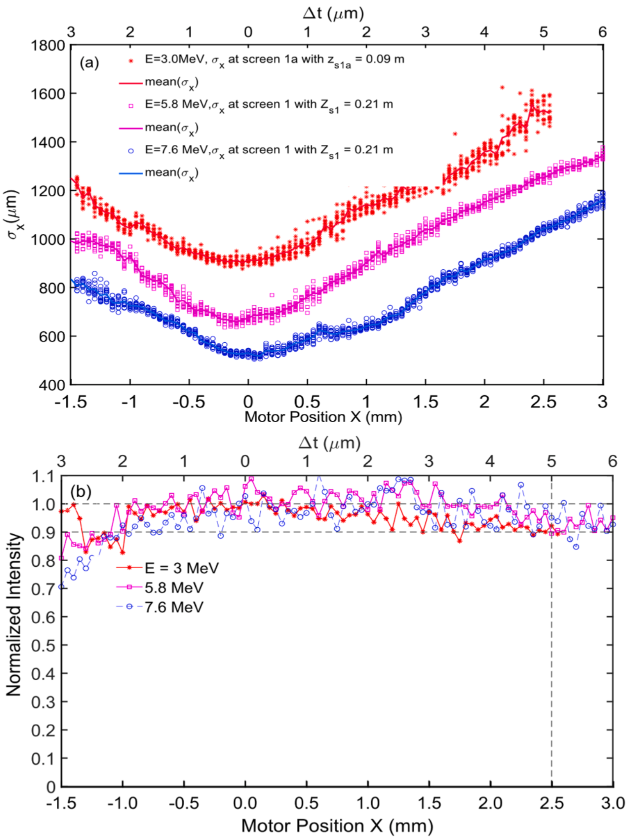

Fig. 3. Beam size and divergence measurements across the wedge-shaped silicon sample. The bottom and top x-axes represent motor position (X) and corresponding sample thickness ($\Delta t = t - t_{min}$), with the thinnest point defined as $t_{min} = 0.2\ \mu m$ and set to $X = 0$ by interferometry. Negative positions appear because the IBF-processed region extended beyond the [0, 15] mm mapping span; however, this side was not intentionally fabricated and is less well controlled, so quantitative analysis is restricted to the positive side. The thickness increment Δt is used throughout. (a) Horizontal beam size $\sigma_x(t)$ for three beam energies: 3.0 MeV (red stars, Screen 1a), 5.8 MeV (magenta squares, Screen 1), and 7.6 MeV (blue circles, Screen 1). Solid lines show average trends; spread reflects statistical uncertainty from ten repeated measurements. (b) Normalized transmitted intensity, defined as the integrated beam intensity transmitted through the sample, normalized to the incident electron beam intensity measured without the sample at the same energy.

above 90 % within the analysis window (t_{min} to $t_{min} + 6$ μm). Within this range, σ_x increases smoothly with thickness while the transmitted intensity remains stable. These measurements provide the experimental input for applying the framework of Section 2.3 to extract divergence rates and benchmark them against analytical and simulation models in Section 2.5.

2.5. Comparison and analysis

Using the framework of Section 2.3, the experimental beam-size data from Section 2.4 were analyzed to extract angular broadening rates and compared with theoretical predictions.

Fig. 4a shows quadratic fits of Eq. (2b) applied to the measured beam-size data for 3.0, 5.8, and 7.6 MeV. The fitted curves reproduce the measurements with R^2 values exceeding 0.98, providing a smooth representation of $\sigma_x(t)^2 - \sigma_x(t_{min})^2$ as a function of thickness. Although the polynomial coefficients (p_1, p_2) have no independent physical meaning, they enable evaluation of the angular divergence rate via Eq. (3).

Fig. 4b presents the extracted divergence rates ($d\Theta/dt$) as a function of Δt for all three energies, compared with predictions from the Highland model (Eq. (5)). At 3.0 MeV, MC simulation results are also

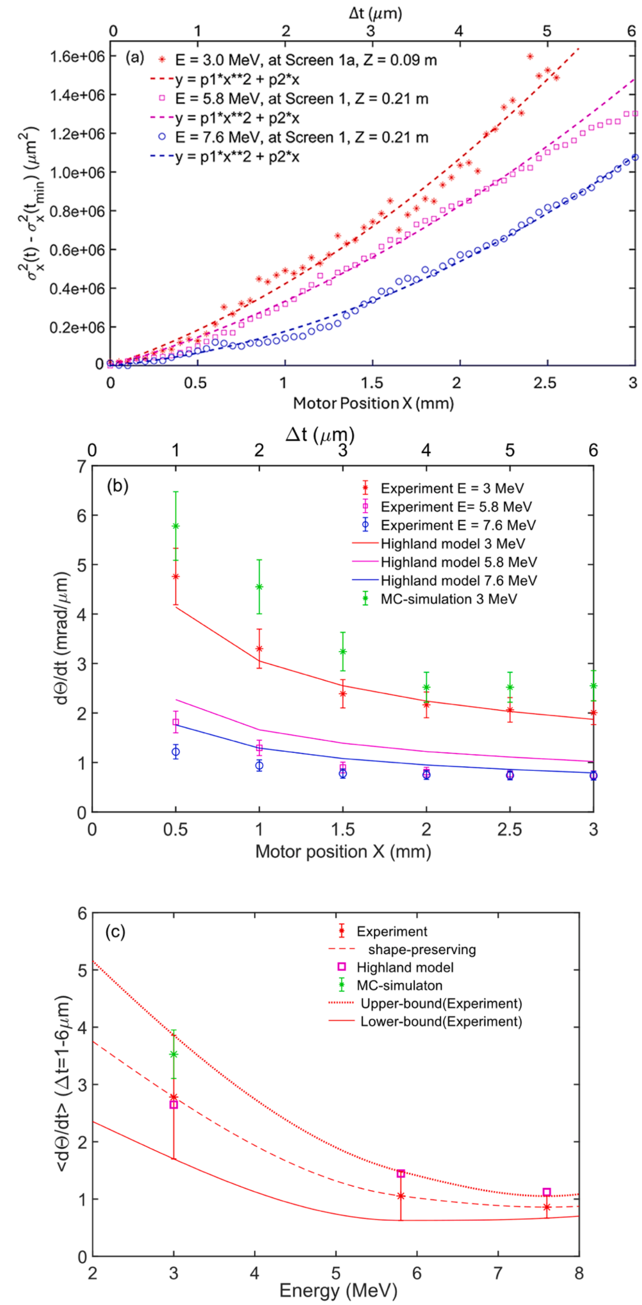

Fig. 4. Extraction and comparison of angular broadening rates. (a) Quadratic fits of Eq. (2b) to beam size data at 3.0, 5.8, and 7.6 MeV. Fitted second-, first- and zeroth-order polynomial coefficients (p_1, p_2, and p_3) are (2.81×10^4, 1.55×10^5, 0.00) for 3.0 MeV, (2.02×10^4, 1.26×10^5, 0.00) for 5.8 MeV, and (2.31×10^4, 4.22×10^4, 0.00) for 7.6 MeV. Corresponding R^2 values that quantify the proportion of the variance in the observed data explained by the fitted model are 0.983, 0.998 and 0.996. (b) Extracted divergence rates $\frac{d\Theta}{dt}$ versus thickness increment Δt, compared with Highland predictions (solid curves) and MC at 3.0 MeV (green stars). Symbols with error bars show experiment. (c) Average divergence rate $\langle d\Theta/dt \rangle$ over $\Delta t = 1$–6 μm. Symbols: red stars (experiment), magenta squares (Highland), green star (MC at 3.0 MeV). Error bars denote spread within the averaging window.

included [28,29]. Experimental values (symbols with error bars) represent mean values with combined statistical and systematic uncertainties (see Section 2.6.1), while MC error bars reflect statistical fluctuations only. Solid curves show the Highland predictions. The data confirm the expected reduction in angular broadening with increasing beam energy, while also revealing systematic offsets: the Highland model underestimates at 3.0 MeV and overestimates at 5.8 and 7.6 MeV, whereas MC overestimates at 3.0 MeV. Because the scattering angle scales as $\sqrt{t}$ (Eq. (4)), even small uncertainties in thickness calibration or wedge gradient can affect accuracy. Additional contributions may arise from beam alignment, finite probe size, detector resolution, or local variations in wedge flatness. Averaging over $\Delta t = 1$–6 μm mitigates the effect of such short-range fluctuations.

Fig. 4c summarizes this energy dependence by showing divergence rates averaged over $\Delta t = 1$–6 μm, the range where transmission remains above 90 % and the data are most reliable. Averaging reduces local fluctuations and yields a single representative value per energy. These results show that while the Highland formula captures the general energy scaling of multiple scattering, its predictive accuracy depends on both beam energy and material properties. Accordingly, the model is more reliable for identifying a practical energy window than for defining a precise optimum value.

Across all energies, both experimental and theory show that angular broadening decreases with increasing beam energy and begins to plateau above ~4 μm thickness. In this regime, raising the beam energy beyond 5.8 MeV provides only modest improvements in spatial resolution, although higher energies extend sample penetration while increasing the likelihood of knock-on displacement damage in crystalline and inorganic materials. These findings emphasize the trade-offs between resolution, penetration, and radiation damage, with the optimal energy window determined by both specimen thickness and composition.

2.6. Derivative-based framework for beam divergence analysis

The agreement between experimental data, analytical models, and MC-simulations (Fig. 4) supports a derivative-based approach: analyzing the rate of change in beam divergence with respect to sample thickness, rather than relying on absolute divergence values. This method offers a key advantage — it reduces sensitivity to variations in initial beam conditions, such as size, divergence, and alignment offsets — making the analysis more robust across different systems and operating conditions.

For the wedged silicon sample, the beam size observed at Screen 1a (for a 3.0 MeV beam) reflects both electron-sample interactions and the initial beam parameters [7,18]. Small trajectory shifts at the sample can displace the apparent position of minimum beam size along the scan axis, complicating interpretation. Aligning the experimental profile such that the minimum beam size corresponds to the thinnest region of the wedge is essential for accurately quantifying scattering-induced broadening. The derivative-based method mitigates sensitivity to such alignment errors, improving both reproducibility and accuracy.

2.6.1. Robustness to initial beam divergence

The detector signal is effectively a convolution of the Gaussian probe with the sample's transmission profile. In samples with smooth, monotonic gradients (e.g., silicon wedges), this convolution averages over local thickness variations, particularly when the probe spans a wide thickness range. Differentiating the signal transforms the problem into a convolution with the derivative of the transmission profile, which suppresses smoothing and enhances sensitivity to local slopes. This restores sensitivity to gradual thickness changes, even with large probes.

In practice, fluctuations in emittance— driven by changes in bunch charge, focusing optics, and energy or phase jitter—lead to variability in beam size and divergence. Emittance values can range from a few picometers in proposed MeV-STEM systems [2] to 10–100 nm in low current operation at existing facilities such as PEGASUS, contributing to uncertainty in the absolute beam divergence. However, analyzing the divergence rate as a function of sample thickness largely suppresses this sensitivity. MC simulations confirm this: increasing the semi-convergence angle from $\sigma_{inc} = 1\ mrad$ to $6\ mrad$ (spanning the PEGASUS operating range) alters the divergence rate by less than 11 %. This weak dependence is reflected in the systematic uncertainty shown in Fig. 4, underscoring the method's applicability across varied beam conditions.

2.6.2. Energy dependence of projected column size in MeV-stem

In STEM, spatial resolution is closely tied to the probe's projected size as it traverses the sample. For thin specimens, the resolution is primarily limited by the focused beam size, which can reach sub-nanometer scales with large convergence angles. In thicker specimens (on the order of several micrometers), however, beam broadening from multiple scattering becomes the dominant factor.

The ultimate resolution can be described as the quadrature sum of three contributions: angular broadening (AB) from convergence angle and sample thickness, emittance and aberration contributions (EC) to the focused probe size, and scattering broadening (SB) from scattering events [7]:

$$\sigma_{\text{tot}} = \sqrt{{\sigma_{\text{AB}}}^2 + {\sigma_{\text{EC}}}^2 + {\sigma_{\text{SB}}}^2}. \tag{6}$$

With the probe focused at the specimen entrance ($t_f = 0$) within a specimen of thickness T, the angular broadening is $\sigma_{AB}(t) = t\cdot\tan(\alpha) \cong t\cdot\alpha,\ 0 \le t \le T$, where α is the semi-convergence angle. The focused beam size at the waist, dominated by emittance and aberrations, is typically on the order of 1 nm for state-of-the-art electron sources [2].

The scattering broadening term is given by

$$\sigma_{SB}(t) = a\cdot e^{b\cdot\left(\frac{t}{MFP}\right)} + c, \tag{7}$$

where t is the local thickness in micrometers, MFP is the mean free path, and a, b, and c are fitting parameters determined from benchmarking [7] ($a \approx \sigma_{inc}$, the incident beam size in nm; $b \cong 10^3\cdot\theta_{el}(E)$, the elastic scattering angle in radians; and $c \cong 0$). This compact formulation relies only on physically meaningful inputs — θ_{el} and MFP — both directly calibrated from experimental data ($\frac{d\Theta}{dt} \approx \frac{b}{MFP}$). Thus, the predictions shown in Fig. 5 are not generic Highland approximations but empirically grounded projections by both simulation and experiment.

At 6 μm thickness, increasing the beam energy from 3.0 MeV (red curve) to 5.8 MeV (blue curve) reduces the projected probe size by almost an order of magnitude, whereas a further increase to 7.6 MeV (black curve) provides only marginal improvement. This saturation reflects the physics of multiple scattering: the characteristic angle scales as $(\beta\cdot p)^{-1}$, so above ~6 MeV the reduction in angular divergence becomes gradual compared to the pronounced improvement between 3 and 5 MeV. In a MeV-STEM system designed with 2 pm emittance, spatial resolution is therefore limited primarily by scattering-induced broadening. Although higher beam energies can suppress divergence and modestly improve resolution, they also increase system complexity, shielding requirements, and the risk of beam-induced damage.

To highlight this threshold-like behavior, Fig. 5b shows the projected probe size as a continuous function of beam energy at fixed thickness values (2, 4, and 6 μm). These results confirm that while higher energies improve sample penetration and reduce beam spreading, resolution gains become increasingly modest above ~6 MeV. Accordingly, the optimal operating point for MeV-STEM must balance resolution goals against practical design constraints, including accelerator complexity, shielding, and radiation damage.

All predictions in Fig. 5 are for silicon, consistent with the experimental wedge sample used in this study. While the qualitative saturation behavior is general, the quantitative values depend on both the initial beam emittance and the material scattering properties (e.g., radiation length, atomic number). The framework can therefore be readily extended to other materials by incorporating the corresponding scattering parameters.

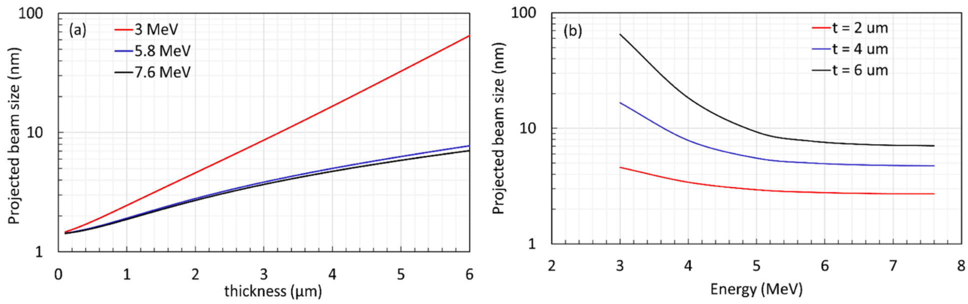

Fig. 5. Projected probe size in a MeV-STEM system with a 2 pm geometric emittance [2], calculated using the empirically fitted model calibrated with experimental divergence rates (Eqs. (1)–3). While such low emittance values represent prospective performance achievable with advanced SRF gun sources [2], developing suitable sources for MeV-STEM remains a non-trivial challenge. (a) Projected beam size σ_{SB} as a function of thickness for beam energies of 3.0 MeV (red), 5.8 MeV (blue), and 7.6 MeV (black), with the probe focused at the sample entrance. At 6 μm thickness, increasing the energy from 3.0 to 5.8 MeV reduces the projected size by nearly an order of magnitude, while further increase to 7.6 MeV yields only marginal improvement. (b) Projected beam size as a function of beam energy for selected thickness values (2, 4, and 6 μm). The results highlight the threshold-like behavior: substantial improvements occur between 3 and 5 MeV, but above ~6 MeV additional energy provides only modest resolution gains, even though electron penetration continues to increase.

3. Conclusion

We developed a standardized experimental platform to quantify energy-dependent electron–sample interactions in thick specimens, using precision-fabricated silicon wedge samples and validated measurements at the PEGASUS beamline. Our results reveal a 2.6-fold reduction in angular broadening between 3.0 and 5.8 MeV, with diminishing improvements above ~6 MeV. This saturation reflects the weak $(\beta{\cdot}p)^{-1}$ scaling of multiple scattering and defines a practical energy window: increasing energy to ~6 MeV substantially improves resolution, while further increases primarily enhance sample penetration at the cost of greater knock-on damage.

These insights have direct implications for MeV-STEM design and applications. In biology, they enable nondestructive imaging of thick tissues such as neuronal circuits or subcellular architectures in their native state, without extensive sectioning. In microelectronics, they support cross-sectional analysis of multilayer integrated circuits and 3D packaging structures, where minimizing preparation artifacts is critical. By clarifying the limits of theoretical models and quantifying energy-dependent trade-offs, this work establishes a benchmark for selecting beam energies in MeV-STEM and provides design guidance for next-generation instruments. Future studies will extend this framework to biological specimens, incorporate radiation-damage considerations, and refine optimal operating regimes for practical applications.

Data availability

The processed data and analysis scripts supporting the findings of this study will be openly available in a public repository upon publication. Additional raw experimental data can be obtained from the corresponding author upon reasonable request, in accordance with DOE's Data Management Plan and FAIR principles.

CRediT authorship contribution statement

Xi Yang: Writing – review & editing, Writing – original draft, Visualization, Validation, Software, Methodology, Investigation, Formal analysis, Data curation, Conceptualization. **Paul Denham:** Writing – review & editing, Writing – original draft, Investigation, Data curation. **Atharva Kulkarni:** Writing – review & editing, Writing – original draft, Software, Data curation. **Brian Schaap:** Writing – review & editing, Writing – original draft, Visualization, Software. **Victor Smaluk:** Writing – review & editing, Writing – original draft, Visualization, Resources, Conceptualization. **Tianyi Wang:** Writing – review & editing, Writing – original draft, Resources, Methodology, Investigation. **Nathalie Bouet:** Writing – review & editing, Writing – original draft, Resources, Methodology. **Mourad Idir:** Writing – review & editing, Writing – original draft, Resources, Methodology. **Pietro Musumeci:** Writing – review & editing, Writing – original draft, Visualization, Validation, Supervision, Resources, Investigation, Formal analysis.

Declaration of competing interest

The authors declare that they have no known competing financial interests or personal relationships that could have appeared to influence the work reported in this paper.

Acknowledges

The authors gratefully thank Lewis Doom and Leo Reffi for providing the 3D-printed box, which was essential for the safe transport of the fragile sample. We also acknowledge Larry Carr and Lei Huang for their assistance with sample thickness characterization, and Timur Shaftan for his invaluable advice, insightful discussions, and guidance throughout the project. This work was partially carried out at the National Synchrotron Light Source II, a U.S. Department of Energy (DOE) Office of Science User Facility operated for the DOE Office of Science by Brookhaven National Laboratory under Contract No. DE-SC0012704. This work was also partially supported by the BNL LDRD 22-029 and BNL LDRD 25024, "DEMAND: Deterministic Manufacturing of strongly curved Diffraction-limited X-ray mirrors".

Supplementary materials

Supplementary material associated with this article can be found, in the online version, at doi:10.1016/j.ultramic.2025.114260.

References

[1] Wang, N.S. *Cell fractionation based on density gradient*, https://user.eng.umd.edu/~nsw/ench485/lab10.htm (2023).

[2] X. Yang, et al., Towards construction of a novel nanometer-resolution MeV-STEM for imaging of thick frozen biological samples, Photonics 11 (3) (2024) 252, https://doi.org/10.3390/photonics11030252.

[3] E. Weiner, J.M. Pinskey, D. Nicastro, M.S. Otegui, Electron microscopy for imaging organelles in plants and algae, Plant Physiol. 188 (2022) 713–725, https://doi.org/10.1093/plphys/kiab449.

[4] J. Böhning, T.A.M. Bharat, Towards high-throughput in situ structural biology using electron cryotomography, Prog. Biophys. Mol. Biol. 160 (2021) 97–103, https://doi.org/10.1016/j.pbiomolbio.2020.05.010.

[5] C.M. Oikonomou, G.J. Jensen, Cellular electron cryotomography: toward structural biology in situ, Annu. Rev. Biochem. 86 (2017) 873–896, https://doi.org/10.1146/annurev-biochem-061516-044741.

[6] M.S. Otegui, J.G. Pennington, Electron tomography in plant cell biology, Microscopy (Oxf) 68 (2019) 69–79, https://doi.org/10.1093/jmicro/dfy133.

[7] X. Yang, L. Wang, V. Smaluk, T. Shaftan, Optimize electron beam energy toward in-situ imaging of large thick frozen bio-samples with nanometer resolution, Nano 14 (9) (2024) 803, https://doi.org/10.3390/nano14090803.
[8] S.G. Wolf, et al., STEM tomography in biology, in: E. Hanssen (Ed.), Cellular Imaging: Electron Tomography and Related Techniques, Springer International Publishing: Cham, 2018, pp. 33–60. Editor.
[9] H. Kohl, L. Reimer, Transmission Electron Microscopy: Physics of Image Formation, Springer-Verlag New York, New York, NY, 2008.
[10] N. Tanaka, Electron Nano-Imaging, 1st edition, Springer, Tokyo, 2017.
[11] M. Du, C. Jacobsen, Relative merits and limiting factors for x-ray and electron microscopy of thick, hydrated organic materials, Ultramicroscopy 184 (2018) 293–309, https://doi.org/10.1016/j.ultramic.2017.10.003.
[12] J.P. Langmore, M.F. Smith, Quantitative energy-filtered electron-microscopy of biological molecules in Ice, Ultramicroscopy 46 (1992) 349–373, https://doi.org/10.1016/0304-3991(92)90024-e.
[13] eds C. Jacobsen, R. Medenwaldt, S. Williams, in: Jürgen Thieme, Günter Schmahl, Dietbert Rudolph, Eberhard Umbach (Eds.), X-Ray Microscopy and Spectromicroscopy: Status Report from the Fifth International Conference, Würzburg, August 19–23, 1996, Springer Berlin Heidelberg, 1998, pp. 197–206. eds.
[14] R.F. Egerton, Choice of operating voltage for a transmission electron microscope, Ultramicroscopy 145 (2014) 85–93, https://doi.org/10.1016/j.ultramic.2013.10.019.
[15] D. Alesini, et al., New technology based on clamping for high gradient radio frequency photogun, Phys. Rev. Special Top.—Accel. Beams 18 (9) (2015) 092001.
[16] R.K. Li, P. Musumeci, Single-shot MeV transmission electron microscopy with picosecond temporal resolution, Phys. Rev. Appl. 2 (2014) 024003.
[17] D. Cesar, et al., Demonstration of single-shot picosecond time-resolved MeV electron imaging using a compact permanent magnet quadrupole based lens, Phys. Rev. Lett. 117 (2016) 024801.
[18] X. Yang, L. Wang, V. Smaluk, et al., Simulation study of high-precision characterization of MeV electron interactions for advanced nano-imaging of thick biological samples and microchips, Nanomaterials 14 (2024) 1797, https://doi.org/10.3390/nano14221797.
[19] T. Wang, et al., Development of a position–velocity–timemodulated two-dimensional ion beam figuring system for synchrotron x-ray mirror fabrication, Appl. Opt. 59 (2020) 3306–3314.
[20] T. Wang, et al., Ion beam figuring system for synchrotron X-ray mirrors achieving sub-0.2-µrad and sub-0.5-nm root mean square, Nanomanuf. Metrol. 6 (2023) 20, https://doi.org/10.1007/s41871-023-00200-x.
[21] https://www.thorlabs.com/thorproduct.cfm?partnumber=XYF1#ad-image-0.
[22] N.J. Harrick, Determination of refractive index and film thickness from interference fringes, Appl. Opt. 10 (1971) 2344–2349, https://doi.org/10.1364/AO.10.002344.
[23] https://www.crytur.com/products/scintillation-screens/.
[24] J.D. Jackson, Classical Electrodynamics, Second Edition, John Wiley & Sons, New York, 1974.
[25] V.L. Highland, Some practical remarks on multiple scattering, Nucl. Instrum. Methods 129 (1975) 497–499, https://doi.org/10.1016/0029-554X(75)90743-0.
[26] Atomic and nuclear properties of silicon (Si), Particle Data Group. https://pdg.lbl.gov/2020/AtomicNuclearProperties/HTML/silicon_Si.html.
[27] Particle Data Group, Passage of particles through matter. In M. Tanabashi et al. (Eds.), Review of Particle Physics (, Phys. Rev. D 98 (3) (2018) 030001, https://doi.org/10.1103/PhysRevD.98.030001.
[28] Liguo Wang, Xi Yang, Monte Carlo simulation of electron interactions in an MeV-STEM for thick frozen biological sample imaging, Appl. Sci. 14 (2024) 1888, https://doi.org/10.3390/app14051888.
[29] B. Quintard, X. Yang, L. Wang, Quantitative modeling of high-energy electron scattering in thick samples using Monte Carlo techniques, Appl. Sci. 15 (2) (2025) 565, https://doi.org/10.3390/app15020565.